IEEE Open Journal of
Power Electronics

Received 8 October 2021; accepted 8 November 2021. Date of publication 11 November 2021;
date of current version 30 November 2021. The review of this paper was arranged by Associate Editor Tommaso Caldognetto.

Digital Object Identifier 10.1109/OJPEL.2021.3127225

Suitability of Current Sensors for the Measurement of Switching Currents in Power Semiconductors

SEBASTIAN SPRUNCK [1], CHRISTIAN LOTTIS [2], FABIAN SCHNABEL [1], AND MARCO JUNG [1,2] (Senior Member, IEEE)

[1] Fraunhofer IEE, Fraunhofer Institute for Energy Economics and Energy System Technology, Kassel 34119, Germany
[2] Bonn-Rhein-Sieg University of Applied Sciences, Sankt Augustin 53757, Germany

CORRESPONDING AUTHOR: SEBASTIAN SPRUNCK (e-mail: sebastian.sprunck@iee.fraunhofer.de)

This work was supported in part by the German Federal Ministry for Economic Affairs and Energy BMWi through the publicly funded research projects SupraGenSys, LEITNING, and PV-MoVe, under Grants FKZ 03EE3010A, 03EI6030D, and 03EE1011B. The authors express their gratitude for this opportunity. Responsibility for the content of this article lies with the authors.

ABSTRACT This paper investigates the impact of current sensors on the measurement of transient currents in fast-switching power semiconductors in a double pulse test (DPT) environment. We review previous research that assesses the influence of current sensors on a DPT circuit through mathematical modeling. The developed selection aids can be used to identify suitable current sensors for transient current measurements of fast-switching power semiconductors and to estimate the error introduced by their insertion into the DPT circuit. Afterwards, this analysis is extended by including further elements from real DPT applications to increase the consistency of the error estimation with practical situations and setups. Both methods are compared and their individual advantages and drawbacks are discussed. Finally, a recommendation on when to use which method is derived.

INDEX TERMS Current measurement, double pulse test, error analysis, measurement errors, power semiconductors, sensor phenomena and characterization, wide band gap.

NOMENCLATURE

$\Delta\iota$	Average error between ι_{DPT} and $\iota_{Filt,k}$
ι_x	Normalised current with respect to I_L
$\iota_{DPT,avg}$	Average value of ι_{DPT} within normalised time interval [0;1]
$\iota_{Filt,k}$	Sensor output signal after application of a k-th order Butterworth filter on ι_{DPT}
Γ_L	Error between the original current i_0 and the DPT current i_{DPT}, introduced through L_{Sensor}
$\Gamma_{\bar{Filt},k}$	Average relative error for a k-th order Butterworth-filtered sensor output signal with respect to the DPT current
Γ_{total}	Total current sensor insertion error
ν	Normalised sensor cutoff frequency
ω_c	Angular sensor cutoff frequency
τ	Normalised time with respect to T_{R0}
$[X]_{[Y],mod}$	Modified function or variable description for the extended error analysis
$\tilde{\nu}$	Normalised angular sensor cutoff frequency
$\varepsilon(\tau)$	Unit Step or Heaviside function
C	DC-Link Capacitor
DPT	Double Pulse Test
DUT	Device Under Test
E_C	Capacitive energy stored in the DC-Link capacitance of a DPT setup
E_L	Inductive energy stored in the storage inductance of a DPT setup
f_c	Sensor cutoff frequency
f_{ref}	Reference frequency for Laplace-domain calculations
H_k	k-th order Butterworth filter

i_0	Original switching current of an unaltered circuit, modeled tangential to the steepest part of a real (nonlinear) switching current
I_L	Current stored in L_{DPT} at the end of the first pulse
i_{DPT}	DPT switching current influenced by L_{Sensor}
L_{Cx}	Parasitic interconnection inductance between the DC-Link capacitor and the power semiconductor half-bridge
L_{DPT}	DPT Storage Inductance
L_{DUT}	Parasitic DUT device inductance
L_{ESL}	Equivalent Series Inductance of the DC-Link capacitor
L_{par}	Sum of all parasitic circuit inductances
L_{Sensor}	Parasitic sensor inductance
m_0/m_1	Current slope modificators to account for the influence of the storage inductor on the original / DPT current
s	Laplace variable
T_{R0}	Current rise time for i_0 to reach I_L
T_{R1}	Current rise time for i_{DPT} to reach I_L
T_{R2}	Rise time for the sensor output signal to reach I_L
V_{DC}	DC-Link Voltage

I. INTRODUCTION

Measuring and minimising wide band gap (WBG) semiconductor switching losses has been a research topic for several years. Numerous groups have investigated the influence of fast $^{dv}/_{dt}$ and $^{di}/_{dt}$ transients on the WBG devices themselves as well as on peripheral components. Drivers and their respective gate networks, but also electromagnetic interference (EMI) radiation have been researched in this regard.

Due to these fast transients, the implementation of WBG devices presents difficult challenges on multiple topics. Besides the higher precision required in terms of timing and component tolerances, bot the design of printed circuit board (PCB) and the measurement of switching losses, among others, require more attention than is the case with conventional Silicon (Si) technology.

As WBG semiconductors become smaller, both of these latter aspects – PCB design and switching loss measurements – are increasingly affected by parasitic circuit elements. In this paper, we focus on the measurement of WBG semiconductor switching losses, especially for very fast devices such as those based on Gallium Nitride (GaN), using the widely accepted Double Pulse Test (DPT). As of today, two main problems regarding the measurement of fast transients can be identified:

1) Capacitive coupling between the measurement equipment and the device under test (DUT), influenced by steep $^{dv}/_{dt}$ slopes easily exceeding 100 V/ns [1].
2) Alteration of the commutation inductance of the circuit due to the inserted current sensor in the current path of the DUT [2], influenced by steep $^{di}/_{dt}$ slopes in the range of several tens or even hundreds A/ns.

The switching times of WBG devices can lie in the range of a few 10 ns [3], [4] or – in the case of low voltage GaN semiconductors – even below 1 ns [5]. In order to accurately measure such fast switching events in a DPT, the applied sensors require bandwidths of at least several hundred MHz, if not GHz.

To enable such fast switching times without generating excessive turn-off overvoltages, the commutation inductances of WBG semiconductors have to be drastically minimised compared to when using conventional Si technology. This inductance minimisation is strongly dependent on the size and shape of the DUT, but can be achieved through appropriate measures described in literature, e.g. [6] – [9].

With these requirements, it is evident that not only the parasitic coupling of sensors towards the DUT circuit, but also the bandwidth of the sensor can limit the accuracy of the measured data. It is well known among power electronic system designers that these properties, among others, are crucial to successfully measuring switching losses and some teams have developed improved sensors with increased cutoff frequencies and/or lower parasitic influences [10], [11] compared to commercial products. Although these developments are definitely helpful and do target key problems in WBG switching loss measurements, the general differences between WBG DPT setups and real applications without current sensors, as well as quantifying these differences, have not yet been presented in international literature.

In a recently published investigation [12], a mathematical description of these differences and an analysis of the magnitude of their impact was presented. In this paper, a summary of this work is first given in Section II. Following this, improved methods are developed in Section III on how best to account for the inevitable influence of the sensor on the DUT, taking into account additional circuit and measurement parameters. Section IV compares the developed methods regarding their usefulness for practical applications. Section V summarises the results and provides an outlook onto further research topics.

II. SUMMARISED TRANSLATION OF PREVIOUS INVESTIGATION

A previous investigation [12] analysed the discrepancies between an unchanged setup, i.e. an application without a current sensor in the commutation path of the current, and a DPT setup requiring such a current sensor (Fig. 1). Two main aspects of interest regarding the current measurement were identified:

1) The alteration of the commutation inductance for the switching current due to the insertion of the current sensor.
2) The transformation of the sensor current into a measurable sensor output voltage.

The qualitative difference between these currents and the output signal are illustrated in Fig. 2. The mechanisms and effects of these aspects are explained below.

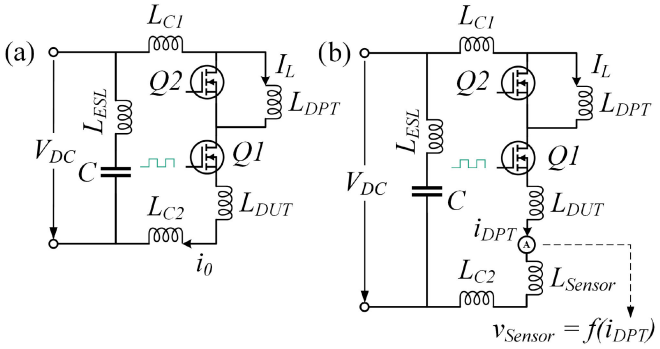

FIGURE 1. Schematic setups with lumped parasitic inductances. a) Original circuit without current sensor. b) DPT setup with added current sensor.

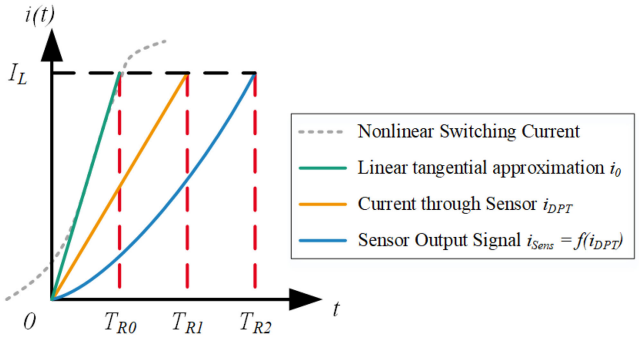

FIGURE 2. Illustration of the qualitative comparison between a turn-on current in an unchanged circuit (green, see Fig. 1a) and the current through the same device, but with an inserted current sensor in a DPT environment (orange, see Fig. 1b) and the output signal of the sensor (blue).

A. ALTERATION OF THE CURRENT PATH

If an intrusive sensor such as a current shunt is used, then its insertion into the source path of the DUT adds parasitic inductance to the commutation loop of the current (L_{Sensor} in Fig. 1(b)). On the other hand, if a sensor such as a Rogowski coil can be wound around exposed device contacts, then it does not require an alteration to the original commutation loop and therefore does not directly insert parasitic inductance to the circuit. Such a situation is often present when investigating power semiconductors in leaded packages or modules. However, even Rogowski coils may require an alteration to the original commutation loop if the circuit is very compact and/or employs a low-inductance design. In high-frequency GaN converters, exposed leads are rarely available so that when trying to measure the switching losses of these devices it can generally be expected that the path of the current will alter.

The reviewed study is based on the assumption that the DC link voltage V_{DC} is virtually constant over the duration of a single DPT. This assumption is valid if the energy E_C stored in the DC link capacitance C is much greater than the energy E_L reqired in the DPT storage inductor L_{DPT} to charge it to the highest desired current $I_{L,max}$:

$$E_C \quad E_L \tag{1}$$

$$\frac{1}{2} C V_{DC}^2 \quad \frac{1}{2} L_{DPT} I_{L,max}^2 \tag{2}$$

$$C \quad L_{DPT} \left(\frac{I_{L,max}}{V_{DC}} \right)^2. \tag{3}$$

This study focused on the worst-case impact of the sensor on very fast-switching circuits and therefore neglects the on-resistance of the semiconductors, the influence of the gate network on the switching event as well as the nonlinearity of the switching current during the commutation process. The switching current is instead approximated as a linear function, tangential to the steepest part of the nonlinear switching current, as illustrated in Fig. 2 (green line). This approximation will certainly exaggerate any following error calculations, but serves well as a worst-case error estimation through the tangential fit to the steepest $^{di}/_{dt}$. Ideal switches were assumed, having a switching time which is limited only by the parasitic commutation loop inductance and the driving voltage of the circuit. For this situation, the description of the DUT current $i_0(t)$ in a setup *without* a current sensor can be approximated by (4):

$$i_0(t) = \frac{1}{L_{par}} \int v(t)\, dt \approx \frac{V_{DC}}{L_{par}} \cdot t \tag{4}$$

where

$$0 \leq t \leq T_{R0} \tag{5}$$

and

$$L_{par} = L_{ESL} + L_{C1} + L_{C2} + L_{DUT} \tag{6}$$

and

$$I_L \stackrel{!}{=} i_0(T_{R0}) = \frac{V_{DC}}{L_{par}} \cdot T_{R0}. \tag{7}$$

This linear approximation is valid up to the time T_{R0} (see Fig. 2) when the semiconductor current i_0 reaches the current I_L that is stored in the storage inductor L_{DPT}, i.e. the time when the load current has completely commutated into the channel of the DUT. For this investigation T_{R0} can be calculated using (7), transformed to (8):

$$T_{R0} = \frac{I_L L_{par}}{V_{DC}}. \tag{8}$$

In real applications, T_{R0} does not solely depend on these variables, but is also influenced by the physical structure of the semiconductor, its gate circuit and the temperature of the chip, among other factors. We deliberately select this simple calculation to determine a worst-case estimate of the errors that have to be expected between real applications and DPT circuits.

When a current sensor is now inserted into the circuit of Fig. 1(a) to provide the DPT environment shown in Fig. 1(b), the total commutation loop inductance is increased by the parasitic inductance of the sensor L_{Sensor}. The current through

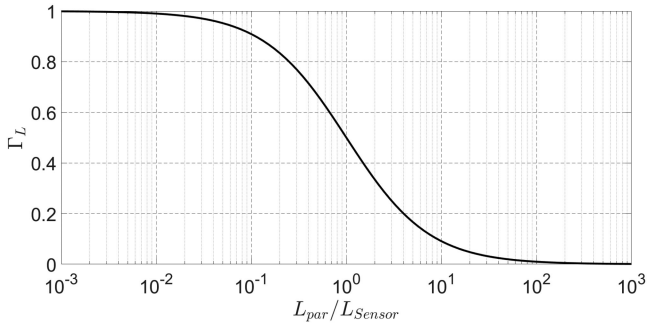

FIGURE 3. Development of the current path alteration error Γ_L according to (13), depending on the ratio of the original setup inductance L_{par} and the sensor inductance L_{Sensor}.

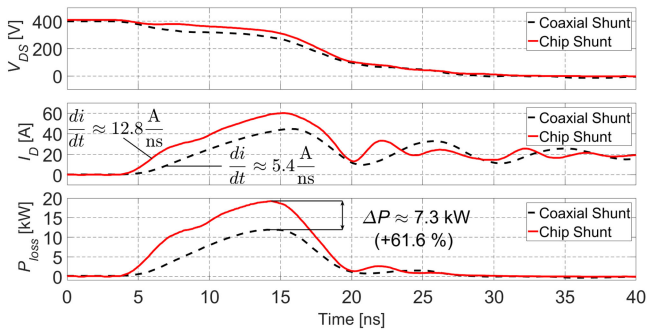

FIGURE 4. Hard-switching turn-on measurements of two identical GaN Systems GS66516T E-HEMT half bridges at $V_{DS} = 400$ V and $I_D = 20$ A with different current sensors, see Fig. 5. Black dashed line: T&M Research SDN-414-10 coaxial shunt with $f_c = 2$ GHz [13] and $L_{Sensor} = 5.4$ nH [2]. Red solid line: 0603 SMD thin-film chip resistors, mounted vertically through the PCB with an FEM-calculated $L_{Sensor} = 48.2$ pH [12]. Each DUT was identical except for the current sensor and its signal connector. Measurement data taken from [12].

the DUT therefore shows a decreased slope compared to (4):

$$i_{DPT}(t) \approx \frac{V_{DC}}{L_{par} + L_{Sensor}} \cdot t \tag{9}$$

where

$$0 \leq t \leq T_{R1} \tag{10}$$

and

$$I_L \stackrel{!}{=} i_{DPT}(T_{R1}) = \frac{V_{DC}}{L_{par} + L_{Sensor}} \cdot T_{R1}. \tag{11}$$

Thus, the insertion of the sensor results in a larger rise time $T_{R1} > T_{R0}$ compared to the original setup, since the current takes slightly longer to reach the desired switching current I_L. Similar to (8), T_{R1} can be estimated by transforming (11) to (12):

$$T_{R1} = \frac{I_L\,(L_{par} + L_{Sensor})}{V_{DC}}. \tag{12}$$

The data recorded in [12] show that such an alteration can have drastic effects, as shown in Fig. 4 for two identical GaN halfbridges, measured with different current sensors. The principle drawings of these setups are shown in Fig. 5.

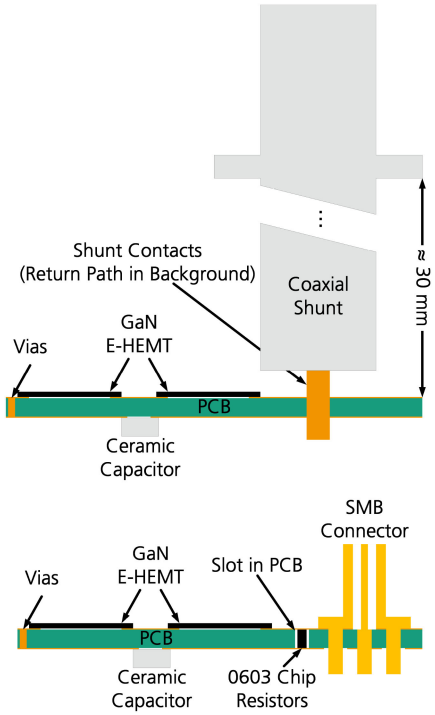

FIGURE 5. Principle drawing of the shunt measurements presented in Fig. 4. Top: Coaxial Shunt. Bottom: Chip Shunt.

If we now consider the timeframe $[0; T_{R0}]$ for the original turn-on current i_0 (see Fig. 2) and compare it to the current of the DPT setup i_{DPT}, we can calculate the relative error Γ_L that describes the difference between these two currents according to (13). For this purpose, the total parasitic inductance L_{par} of the original commutation loop (see (6)) and the parasitic inductance of the sensor L_{Sensor} have to be known:

$$\Gamma_L := \frac{i_0(t) - i_{DPT}(t)}{i_0(t)} = \frac{1}{\frac{L_{par}}{L_{Sensor}} + 1} \tag{13}$$

valid for $0 \leq t \leq T_{R0}$.

The development of this error is depicted in Fig. 3. This error becomes greater when the parasitic inductance of the sensor is large compared to the original setup. When both values are identical, the relative error equals 50 %. In this case, the current through the sensor (Fig. 2, orange curve) can only rise with a $^{di}/_{dt}$ slope half as steep as in the original setup (see (4) and (9)).

This error can be negligible or even zero if no physical alteration of the commutation loop is neccessary and no parasitic sensor inductance is inserted into the circuit ($L_{Sensor} \to 0$). This is commonly possible in larger converters that employ semiconductor modules with screw-in connections. Yet in many compact DPT environments and especially with GaN semiconductors in small packages, this is not the case and an inductive influence of the current sensor should be expected.

The relationship between the paracitic inductances of the DUT and the sensor in (13) emphasises the need for

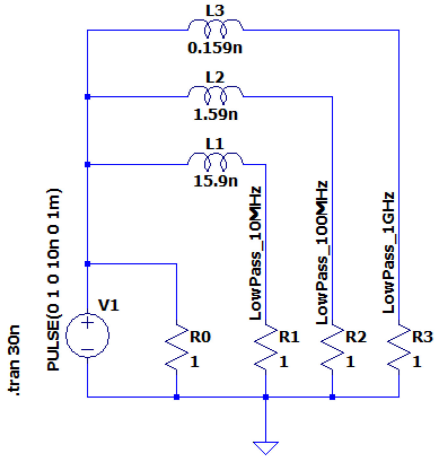

FIGURE 6. LTSPICE-model to simulate the RL filter effect of a shunt current sensor with parasitic inductance for three different cutoff frequencies of 10 MHz, 100 MHz and 1 GHz.

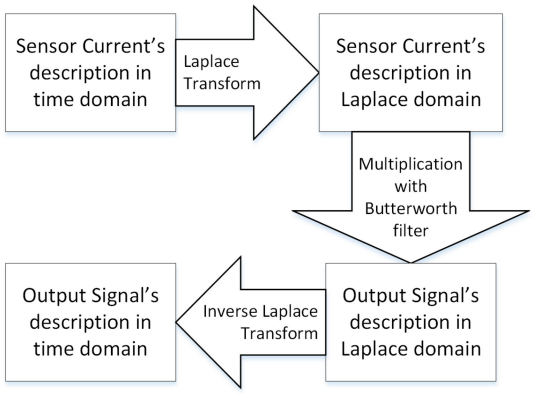

FIGURE 7. Flow chart of the calculation of the filtered signal through the description of the sensor current and a Butterworth filter.

extremely small and low inductive current sensors for highly optimised circuits, such as those often found in high-frequency, fast-switching WBG applications. It hast to be considered, however, that this error always depends on the *ratio* of these inductances, not on the absolute value of one of them: A greater error can be expected not only for geometrically small setups common to WBG applications, but also for larger converters that adopt a large current sensor for which the commutation loop has to be altered.

B. DISTORTION OF THE SENSOR OUTPUT SIGNAL

In order to record a measurement signal from the current sensor, the current flowing through it has to be converted into a voltage signal that can be recorded by a data logger. As no sensor exists that can directly measure a current, this conversion is unavoidable and has to be accounted for in any sensor. This conversion imposes a filter characteristic on the current waveform (9). Its effect depends on the type of sensor, e.g. resistive shunt, hall effect, or Rogowski coil, as well as on its physical composition, i.e. materials, size and shape. The type of the filter typically shows low-pass characteristic, though band-pass behaviour is not uncommon either.

A simple LTSPICE simulation, shown in Fig. 6 and Fig. 8, validated this filter effect. It can be described by a Butterworth filter, as this type of filter is designed for a flat amplitude gain below its cutoff frequency. This behaviour is desirable for high-bandwidth current and voltage probes, since non-flat amplitude gain would distort the measurement of high-frequency components and therefore produce inaccurate results. The mathematical description of a Butterworth filter thus fits the desired filter behaviour of most probes used in a DPT setup.

We can account for the filter effect of the sensor on high-frequency components of the current by selecting an appropriate Butterworth filter and by applying the cutoff frequency of the sensor f_c to it. Applying such a filter onto the current is mathematically equivalent to convolving (9) with the time domain function of the filter. However, it is simpler to first transform (9) into the Laplace domain, where a convolution becomes a simple multiplication, and then transform the product of this multiplication back into the time domain for further analysis. Fig. 7 shows the flow chart of this approach.

Since (9) gives a linear current slope, we can interpret and further analyse it in a normalised form that simplifies the following mathematical investigations. To do this, we first normalise (9) by its amplitude I_L (11), as shown in (14).

$$\iota_{DPT}(t) := \frac{i_{DPT}(t)}{I_L} = \frac{t}{T_{R1}} \tag{14}$$

We then combine the result of (14) into a single, unitless variable τ (15), which essentially normalises the time domain with respect to the current rise time T_{R1}.

$$\iota_{DPT}(\tau) = \tau \tag{15}$$

where

$$\tau := \frac{t}{T_{R1}} \tag{16}$$

We continue to use (15) and therefore also consider the filter description in a normalised form with respect to reference frequency f_{ref} (17) that is the inverse of the DPT current rise time T_{R1} (see Fig. 2).

$$f_{ref} := \frac{1}{T_{R1}} \tag{17}$$

The normalised sensor cutoff frequency ν and the corresponding normalised angular frequency $\tilde{\nu}$ can therefore be defined as:

$$\nu := \frac{f_c}{f_{ref}} = f_c T_{R1} \tag{18}$$

$$\tilde{\nu} = 2\pi\nu = 2\pi f_c T_{R1}. \tag{19}$$

With this normalised angular frequency, the normalised Laplace-domain description for a first-order Butterworth low-pass filter $H_1(\tilde{\nu})$ can be expressed as (20), where s is the

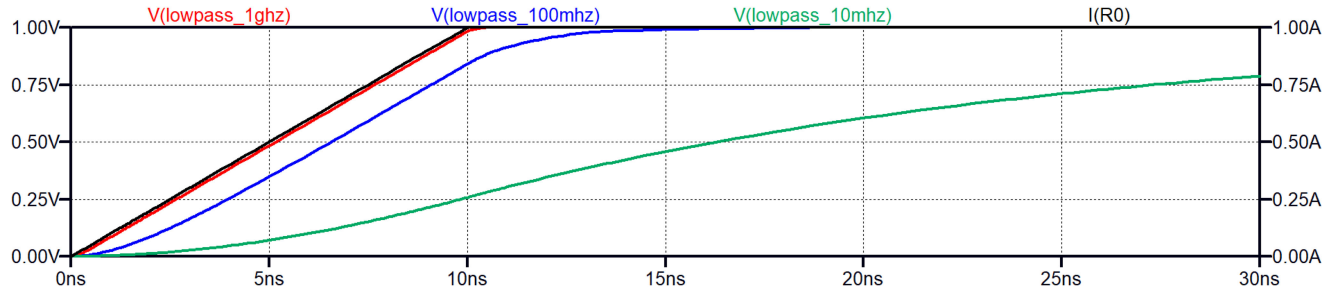

FIGURE 8. Results of the LTSPICE-Simulation shown in Fig. 6 for a current rise time of $T_{R1} = 10$ ns (black curve). The voltage measured across current shunt R_1 (lowest cutoff frequency, dark green curve) shows a large discrepancy compared to the ideal current. The higher the cutoff frequency (R_2 and R_3, blue and red curve), the closer the similarity between the measured signal and the real current.

laplace variable.

$$H_1(\tilde{\nu}) = \frac{1}{\frac{s}{\tilde{\nu}} + 1} \tag{20}$$

By applying the above transformation method (see Fig. 7), we obtain the normalised sensor output waveform description as a function of normalised time τ and the normalised angular cutoff frequency of the sensor $\tilde{\nu}$. For a first-order Butterworth filter, the sensor output signal $\iota_{Filt,1}$ is given by:

$$\iota_{Filt,1}(\tau, \tilde{\nu}) = \frac{e^{-\tilde{\nu}\tau} + \tilde{\nu}\tau - 1}{\tilde{\nu}}. \tag{21}$$

Since we now have mathematical descriptions for both the normalised sensor current (15) and the normalised sensor output signal (21), we are able to develop an error description to quantify the filter error of the sensor. Unlike (13), a direct relative error description between these two signals is time-dependent, which is undesirable for a quick comparison between different sensors. As an alternative, we can calculate the relation between the average error and the average value of the sensor current over the normalised time interval [0;1] ([0;T_{R1}] in the non-normalised description). The average error $\Delta\iota$ is calculated by (22), while the average value of the sensor current $\iota_{DPT,avg}$ is given by (23). In both cases, the averaging is implicit in the normalisation of time, see (14) and (15).

$$\begin{aligned}\Delta\iota(\tilde{\nu}) &:= \int_0^1 |\iota_{DPT}(\tau) - \iota_{Filt,1}(\tau, \tilde{\nu})|\, d\tau \\ &= \int_0^1 \frac{1 - e^{-\tilde{\nu}\tau}}{\tilde{\nu}}\, d\tau = \frac{e^{-\tilde{\nu}} + \tilde{\nu} - 1}{\tilde{\nu}^2}\end{aligned} \tag{22}$$

$$\begin{aligned}\iota_{DPT,avg} &:= \int_0^1 \iota_{DPT}(\tau)\, d\tau \\ &= \int_0^1 \tau\, d\tau = \frac{1}{2}\end{aligned} \tag{23}$$

The average relative filter error for a first-order Butterworth filter can now be calculated as the ratio of (22) and (23):

$$\Gamma_{Filt,1}(\tilde{\nu}) = \frac{\Delta\iota(\tilde{\nu})}{\iota_{DPT,avg}} = \frac{2\left(e^{-\tilde{\nu}} + \tilde{\nu} - 1\right)}{\tilde{\nu}^2}. \tag{24}$$

The error $\Gamma_{Filt,1}$ can be interpreted geometrically as the ratio of the area between the respective curves and the area below the sensor current ι_{DPT} (see Fig. 2).

Substituting (19) into (24), we obtain the non-normalised error description of the sensor's filter effect, which depends on its angular cutoff frequency ω_c and the DPT current rise time T_{R1}:

$$\Gamma_{Filt,1}(\omega_c,\, T_{R1}) = \frac{2\left(e^{-\omega_c T_{R1}} + \omega_c T_{R1} - 1\right)}{(\omega_c T_{R1})^2}. \tag{25}$$

Note that T_{R1} is the rise time of the DPT current and *not* the measured rise time of the sensor output. In practical applications, it is impossible to measure T_{R1}, since a direct current measurement is not possible with available technology. We must therefore resort to an approximation through (12), which again makes (25) a worst-case estimate for the filter error of the sensor.

Error descriptions for higher filter orders can be calculated in the same manner by replacing (20) with the description of a Butterworth filter of the desired order. A second-order Butterworth filter is also analysed in [12].

C. TOTAL SENSOR ERROR

The influences described in Sections II-A and II-B build on each other and form a chain of errors. After inserting the current sensor into the circuit, the similarity between the DPT current i_{DPT} and the original current i_0 is reduced by the inductance insertion error Γ_L (13). The remaining similarity is then again reduced by the filter error of the sensor $\Gamma_{Filt,1}$ (25) or a suitable description for higher filter orders. The total error between the output signal and the original current is calculated according to (26).

$$\begin{aligned}\Gamma_{total} &= 1 - (1 - \Gamma_L) \cdot (1 - \Gamma_{Filt,1}) \\ &= \Gamma_L + \Gamma_{Filt,1} - \Gamma_L \cdot \Gamma_{Filt,1}\end{aligned} \tag{26}$$

This total error must not be confused with the total error of the DPT switching loss measurement, as (26) relates only to the current measurement. This description accounts for the parasitic commutation inductance of the original circuit L_{par}, the sensor's parasitic inductance L_{Sensor}, its bandwidth f_c and the switching time of the semiconductor T_{R1}. This enables the analysis of transient current sensors with regard to their total

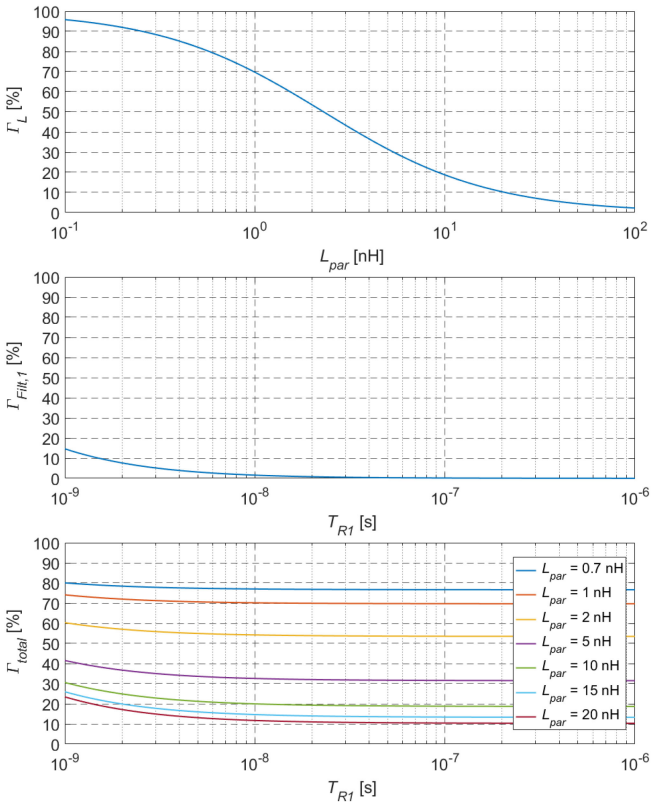

FIGURE 9. **Error calculations for a coaxial shunt with $f_c = 2$ GHz [13] and $L_{Sensor} = 2.3$ nH [2]. Top: Parasitic inductance error. Middle: First-order Butterworth sensor filter error. Bottom: Resulting total error. Figure adapted from [12].**

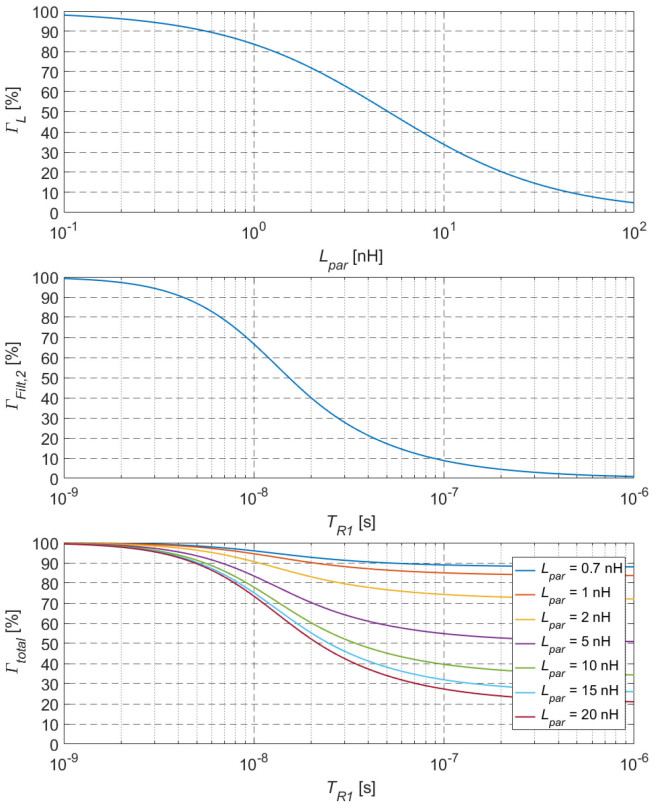

FIGURE 10. **Error calculations for a Rogowski coil with $f_c = 50$ MHz [14] and $L_{Sensor} = 5.1$ nH for a supposed loop around the coil [12]. Top: Parasitic inductance error. Middle: Second-order Butterworth sensor filter error. Bottom: Resulting total error. Figure adapted from [12].**

influence on switching loss measurements of power semiconductors and even the generation of selection aids. This has already been performed in [12] for a number of commercial and experimental current sensors. Two examples are shown in Fig. 9 and Fig. 10 .

The parameters on which the total sensor error Γ_{total} (26) depends are either sensor-related or circuit-related. The sensor-related parameters L_{Sensor} and f_c are fixed on a per-sensor basis, while the circuit-related parameters L_{par} and T_{R1} can vary widely, depending on the application. Each sensor therefore generates a three-dimensional error function $\Gamma_{total} = f(L_{par}, T_{R1})$ according to (26). Since it is relatively difficult to visualise and interpret such three-dimensional graphs for multiple sensors in a combined figure, we resort to two-dimensional cross-sections of these functions to enable a comparison between different sensors.

This can be achieved by defining acceptable total error values and by plotting the cross-sectional contour lines for the error calculation of each sensor. The resulting figure is then dependent on L_{par} and T_{R1}. By repeating this approach for different acceptable error values, e.g. 10 %, 5 % and 1 %, a quick selection aid for suitable sensors can be created with respect to the desired DPT environment. This was performed in [12] for a number of available and experimental current sensors; an excerpt is presented in Fig. 12 and Fig. 13.

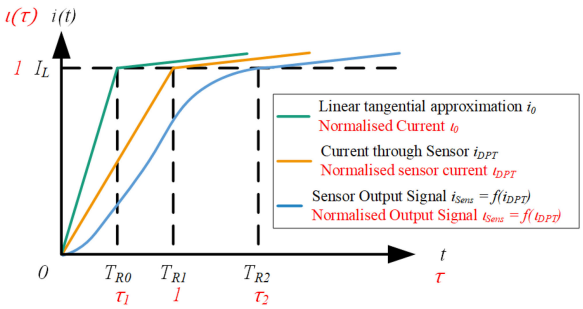

FIGURE 11. **Expansion of Fig. 2 to include the total turn-on currents. Before the currents reach the DPT storage inductor current I_L, their slope is determined by L_{par}. Afterwards, they are limited by $L_{DPT} >> L_{par}$. *Black Labels:* Time-dependent current descriptions. *Red Labels:* Normalised mathematical functions.**

The marked lines represent the contours where the respective current sensor produces a total error that is identical to the one investigated – 10 % in Fig. 12 and 5 % in Fig. 13 – while a DPT setup operating to the left or below these lines, i.e. with either faster switching time T_{R1} or a lower parasitic setup inductance L_{par}, is subject to a larger error. Points to the left or above these lines (slower switching time or larger setup inductance) have lower errors than those examined through these figures.

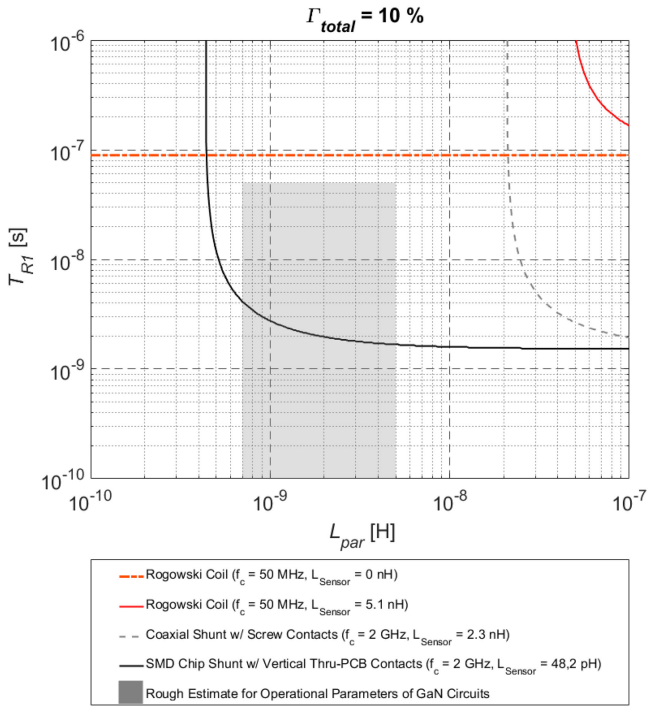

FIGURE 12. Cross-sectional view of the three-dimensional error functions at a height of $\Gamma_{total} = 10\,\%$ for different sensors. Orange dash-dotted line: Rogowski coil [14] wound around an accessible conductor so that no parasitic sensor inductance is inserted into the circuit. Red solid line: The same Rogowski coil, but with $L_{Sensor} = 5.1$ nH inserted into the circuit. Gray dashed line: Coaxial Shunt [13] with screw contacts of $L_{Sensor} = 2.3$ nH. Black solid line: SMD chip shunt as developed in [12] with $L_{Sensor} = 48.2$ pH. Figure adapted from [12].

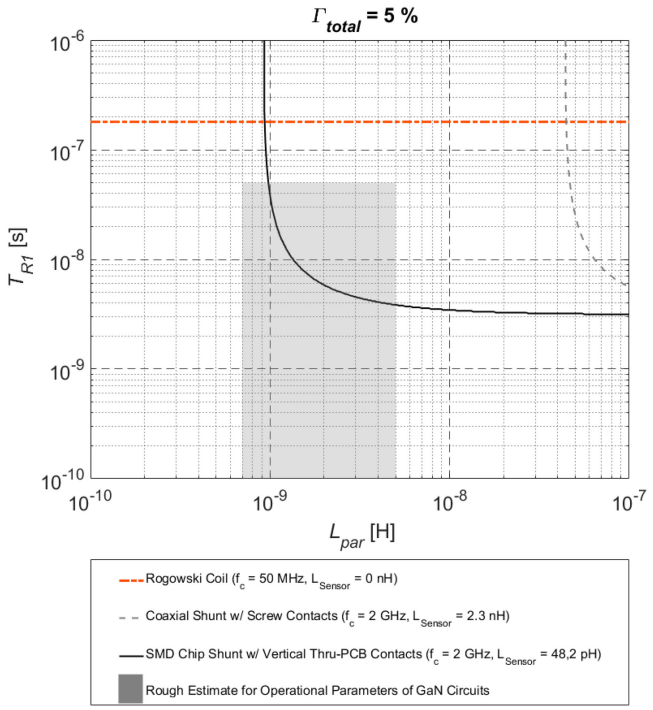

FIGURE 13. The same evaluation as presented in Fig. 12, but with a cross-sectional height of $\Gamma_{total} = 5\,\%$. A Rogowski coil with an inserted $L_{Sensor} = 5.1$ nH cannot produce such low errors in the investigated parameter range (L_{par}, T_{R1}) and is therefore not visible in this graph. Figure adapted from [12].

III. EXPANSION OF THE PROPOSED SENSOR EVALUATION METHODOLOGY

The proposed error estimation can readily be used to compare the effect of different sensors on a given application and to rate them according their influence upon it. However, the approach presented in Section II does not consider the entire switching process in a DPT environment. As can be seen in Fig. 2, the integration interval of (24) is chosen to end at the time T_{R1} when the current of the DPT circuit i_{DPT} reaches the load current I_L, stored in the DPT inductor L_{DPT}.

Yet in a real DPT setup, we have no possibility of measuring the true value of i_{DPT} without applying the sensor's filter effect described in Section II-B. We can therefore only use the measurement signal i_{Sens} to discern the operating conditions for the DUT (current-wise) and we need to find an error description that takes the difference in rise times into account if we want to make such an analysis viable for practical applications.

If, on the other hand, we extend the time frame of the error calculation up to the time when i_{Sens} reaches I_L, then both the real sensor current i_{DPT} as well as the original switching current i_0 already have a higher value at this time, depending on the DPT storage inductor L_{DPT}. This means that a new error description must also account for the different amplitudes of the currents for times $t > T_{R1}$ ($\tau > 1$).

A. TIMEFRAME AND AMPLITUDE EXPANSION

The following considerations are based on the extended signals depicted in Fig. 11. After the current i_0 in the original setup reaches I_L at $t = T_{R0}$ (τ_1 in the normalised analysis), its slope is no longer dominated by the commutation inductance L_{par} of the setup (see (6)), but instead by the DPT storage inductor L_{DPT}. This storage inductor is typically many orders of magnitude larger than the commutation loop inductance ($L_{DPT} >> L_{par}$), leading to a sharp decrease in the slope for i_0 at times $t > T_{R0}$ ($\tau > \tau_1$).

Following the normalised analysis of the previous investigation in Section II, we can mathematically describe this behaviour through (27) by combining two unit step (or Heaviside) functions $\varepsilon(\tau)$, which can be used to represent the change of slope with respect to time by modifying their function arguments, as mentioned above. The first term describes the slope of the signal up to normalised time τ_1, while the second term modifies this slope by the factor m_0 to account for the influence of L_{DPT} on ι_0 for $\tau \geq \tau_1$.

$$\iota_{0,mod}(\tau) = \frac{\tau}{\tau_1} \cdot \varepsilon\left(\frac{\tau}{\tau_1}\right) - m_0 \cdot (\tau - \tau_1) \cdot \varepsilon(\tau - \tau_1) \quad (27)$$

where

$$m_0 = 1 - \frac{L_{par}}{L_{par} + L_{DPT}}. \quad (28)$$

The same logic applies to the normalised sensor current ι_{DPT} of the DPT measurement setup, although this current

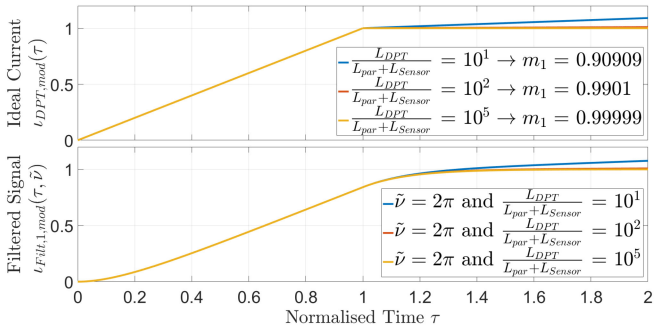

FIGURE 14. Calculated DPT currents $\iota_{DPT,mod}$ according to (29) for different inductance ratios $\iota_{DPT}/(\iota_{par}+\iota_{Sensor})$ (top) and the respective calculated sensor output signals $\iota_{Filt,1,mod}$ for $\nu = 1$ ($\tilde{\nu} = 2\pi$) according to (31).

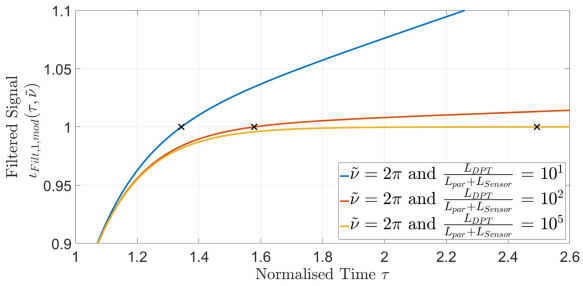

FIGURE 15. Magnification of the lower graph of Fig. 14, displaying the dependency of τ_2 – the time at which the output signal reaches the load current, marked by black crosses – on the inductance ratio $\iota_{DPT}/(\iota_{par}+\iota_{Sensor})$.

requires a slightly larger time $T_{R1} > T_{R0}$ ($\tau = 1 > \tau_1$) to reach the desired current, due to the added parasitic sensor inductance L_{Sensor}. Therefore, the $^{di}/_{dt}$ slope of ι_{DPT} does not change for $\tau > \tau_1$, but for $\tau > 1$, according to (29):

$$\iota_{DPT,mod}(\tau) = \tau \cdot \varepsilon(\tau) - m_1 \cdot (\tau - 1) \cdot \varepsilon(\tau - 1) \tag{29}$$

where

$$m_1 = 1 - \frac{L_{par} + L_{Sensor}}{L_{par} + L_{Sensor} + L_{DPT}}. \tag{30}$$

As described in Section II-B, the sensor imposes a low-pass filter on $\iota_{DPT,mod}$, resulting in a further increase in rise time $T_{R2} > T_{R1}$ ($\tau_2 > 1$) for its output signal ι_{Sens} to reach the switching current. It is important to notice that not only the initial current commutation up to T_{R1}, but also the following (slower) current rise due to the DPT storage inductor affects the filtered output signal. Since sharp waveform changes are smoothed by low-pass filters, this delay therefore depends on the cutoff frequency of the filter f_c (ν in the normalised description) and on the ratio of the parasitic sensor inductance and the storage inductance. Unlike $\iota_{0,mod}$ and $\iota_{DPT,mod}$, the slope for the sensor output signal does not exhibit a sudden change due to this low-pass distortion and instead asymptotically approaches the slope allowed by the driving DC-Link voltage V_{DC} and the storage inductor L_{DPT}.

For a first-order Butterworth low-pass filter, we can calculate the extended sensor output signal $\iota_{Filt,1,mod}$ by the same transformation process described in Section II-B (Fig. 7), using the modified DPT current (29):

$$\begin{aligned}\iota_{Filt,1,mod}(\tau, \tilde{\nu}) := {} & \frac{e^{-\tilde{\nu}\tau} + \tilde{\nu}\tau - 1}{\tilde{\nu}} \cdot \varepsilon(\tau) \\ & - m_1 \frac{e^{-\tilde{\nu}(\tau-1)} + \tilde{\nu}(\tau - 1) - 1}{\tilde{\nu}} \cdot \varepsilon(\tau - 1).\end{aligned} \tag{31}$$

The effect of these extended signals and the corresponding calculated output signals are shown in Fig. 14 and Fig. 15.

B. IMPROVED ERROR CALCULATION

As we now have extended descriptions for both the time and amplitude dependencies of the sensor current $\iota_{DPT,mod}$ as well as for its first-order filtered output signal $\iota_{Filt,1,mod}$, we can construct an improved error calculation compared to (25) and (26).

The setup error Γ_L is not affected by the change of scope described in Section III-A, since its calculation is independent of time, shown in (13). This part of the total error calculation according to (26) can therefore be reused for the expanded error calculation that is to be developed here.

However, we have to make modifications for Γ_{Filt} (24) to account for this new approach. A more realistic error description can be constructed if we consider the difference between the signals (29) and (31) within the timeframe $[0; T_{R2}]$ in Fig. 11. As argued above, it is not possible to calculate a time-independent error due to the low-pass filter effect of the current sensor, but we are able to again calculate the average relative error by arithmetic function averages of the respective current descriptions.

However, we do have to keep in mind the fact that the integration times must be changed, since the difference between the output signal of the sensor and the real current must be taken into account until the output signal $\iota_{Filt,1,mod}$ reaches the desired switching current at $t = T_{R2}$ or, in the normalised description, at $\tau = \tau_2$. On the other hand, the reference value has only to account for the real DPT current and therefore ends at $t = T_{R1}$ ($\tau = 1$). It is therefore identical to (23). Consecutively, the improved average relative error for a first-order Butterworth filter $\Gamma_{Filt,1,mod}$ can be calculated according to (32):

$$\Gamma_{Filt,1,mod}(\tilde{\nu}, \tau_2) := \frac{\Delta\iota_{mod}(\tilde{\nu})}{\iota_{DPT,avg}} \tag{32}$$

where

$$\begin{aligned}\Delta\iota_{mod}(\tilde{\nu}) := {} & \frac{1}{\tau_2} \int_0^{\tau_2} |\iota_{DPT,mod}(\tau) - \iota_{Filt,1,mod}(\tau)|\, d\tau \\ = {} & \frac{e^{-\tilde{\nu}\tau_2} + \tilde{\nu}\tau_2 - 1}{\tilde{\nu}^2} \\ & - m_1 \cdot \frac{e^{-\tilde{\nu}(\tau_2-1)} + \tilde{\nu}(\tau_2 - 1) - 1}{\tilde{\nu}^2}\end{aligned} \tag{33}$$

and

$$\iota_{DPT,avg} = \int_0^1 \iota_{DPT,mod}(\tau)\, d\tau = \frac{1}{2}. \tag{34}$$

Substituting (16) and (19), we obtain non-normalised description (35). As mentioned in Section II-B, error descriptions for higher filter orders, e.g. $\Gamma_{Filt,2,mod}$ for a second-order Butterworth filter, can be calculated by using the corresponding filter descriptions for the transformation process described in Fig. 7.

$$\Gamma_{Filt,1,mod}(\omega_c, T_{R1}, T_{R2}) = \frac{2}{(\omega_c T_{R1})^2} \cdot (A - B) \tag{35}$$

where

$$A = e^{-\omega_c T_{R2}} + \omega_c T_{R2} - 1 \tag{36}$$

and

$$B = m_1 \cdot \left(e^{-\omega_c (T_{R2} - T_{R1})} + \omega_c (T_{R2} - T_{R1}) - 1\right) \tag{37}$$

With these expanded sensor errors, we can now again calculate a total error that accounts for both the inductance of the sensor and its filter effect, similar to (26):

$$\Gamma_{total,mod} = \Gamma_L + \Gamma_{Filt,1,mod} - \Gamma_L \cdot \Gamma_{Filt,1,mod}. \tag{38}$$

Similar to the reviewed error description in Section II, (38) yields the extended error description as a function of the parasitic setup and storage inductances L_{Sensor}, L_{par} and L_{DPT}, the sensor's cutoff frequency f_c, the switching time of the semiconductor T_{R1} and the rise time of the output signal T_{R2}.

IV. METHODOLOGY COMPARISON

Both methods described in Sections II and III take into account both the influence of the sensor on the current itself as well as the sensor's output distortion due to its transfer function. The influence on the current Γ_L is identical in both calculations and has already been presented in Section II-A. Therefore, only the second part of the chain of errors – the filtering effect of the sensor's transfer function – is compared here.

A. ERROR INTERPRETATION

A major difference between the reviewed and the newly proposed filter error calculations (24) and (32) is their possible interpretation. As mentioned in section II-B, the former can be interpreted as the ratio of the area between the curves ι_{DPT} and ι_{Sens} and the area below ι_{DPT}. This is possible due to the identical integration intervals in both the numerator and the denominator of (24). In the newly proposed calculation (32) in Section III-A, this is not directly possible because the integration intervals differ: The numerator expands to the rise time of the filtered output signal ι_{Sens}, i.e. τ_2, while the denominator is limited to $\tau = 1$. This difference may seem insignificant at first sight, but has a profound effect on the error calculation, as very high inductance ratios $L_{DPT}/(L_{par}+L_{Sensor})$ lead to very large rise times τ_2, see Fig. 15. Therefore, the average function value of the numerator in (32) will be lower than in (24), resulting in *lower* calculated errors even though the signal takes *longer* to reach the full load current value I_L.

These lower results should not be confused with actual small measurement errors. If $\tau_2 >> 1$ or, in the non-normalised description, $T_{R2} >> T_{R1}$, then the cutoff frequency of the sensor and/or the inductance ratio is inappropriate for the given task. This undesirable effect is one of the drawbacks of having to resort to average function values and once again emphasises the need to account for the entire measurement setup when trying to measure very fast transient currents.

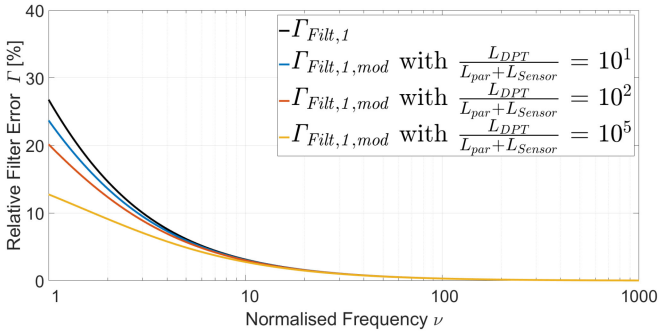

FIGURE 16. Results of the error calculations according to (24) and (32) depending on the normalised sensor cutoff frequencies ν. The different colours compare the dependency of the extended error analysis on different inductance ratios $L_{DPT}/(L_{par}+L_{Sensor})$ against the original analysis of Section II.

B. INFLUENCES ON THE ERROR CALCULATION

A comparison of the described transfer function errors with respect to the normalised sensor cutoff frequency ν (see (18)) is shown in Fig. 16. For large normalised frequencies $\nu \gtrsim 20$, i.e. very slow switching times T_{R1} or very high sensor cutoff frequencies f_c, both calculations result in virtually identical error values. However since $\nu = 20$ still produces errors of $\Gamma_{Filt,1,mod} \approx 1.5 \ldots 1.6\,\%$, the transfer function of the sensor still has a measurable impact on the precision of the switching loss calculation, especially since this error only accounts for part of the total error Γ_{total}.

At lower normalised frequencies, the difference in scope between the reviewed method of Section II and the newly developed method of Section III becomes increasingly apparent. These low normalised frequencies are present if either an unsuitable current sensor is selected for a given switching time or if the switching time of the DUT becomes so fast that its reciprocal value even comes close to the highest available sensor bandwidths ($1/T_{R1} \approx f_c$).

The former can be avoided by choosing a suitable sensor – if one can be found and properly inserted into the DUT circuit – while the latter is almost impossible to deal with usingavailable technology. As stated in Section I, switching times of GaN E-HEMT devices approach single-digit Nanoseconds and therefore require the highest possible sensor cutoff frequencies to provide even normalised frequencies $\nu > 1$. The faster the DUT switches, the larger the error to be expected due to the filter effect of the sensor.

Since a DPT current is a transient signal and not a perodic one, the Whittaker-Kotelnikov-Shannon sampling theorem[1] is

[1] Also known as Nyquist-Shannon sampling theorem, see [15], [16].

not strictly applicable to this investigation, but it is clear from Fig. 16 that it is nevertheless advisible to select bandwidths much larger than twice the reciprocal rise time ($\nu > 2$) to enable low DPT measurement errors Γ_{Filt}. The concrete choice of the sensor's cutoff frequency depends on the tolerable error value and on the available sensors for a given switching time.

C. ADVANTAGES AND DRAWBACKS

The first method presented in Section II-B is mathematically simple and depends only on two circuit properties – the cutoff frequency of the sensor f_c and the switching time of the DUT T_{R1}. Yet this simple approach will certainly overestimate the actual error, as it is based on worst-case approximations and relies on the calculation of the DUT's switching time rather than its measurement. The second approach developed in Sections III-A and III-B improves on these drawbacks but is mathematically more complex. It additionally takes into account both the measurement of the rise time T_{R2} as well as the inductance ratio of the DPT circuit (30). Yet the resulting calculation (35) can lead to implausible results if L_{DPT} $(L_{par} + L_{Sensor})$.

However, L_{DPT} cannot be reduced to arbitrarily low values for two reasons:

1) A certain amount of DPT storage inductance L_{DPT} is required so that the switching current I_L only decreases by a negligible amount between the first and the second pulse.
2) The current resolution that can be applied to the DUT depends on the combination of L_{DPT} and the clock frequency of the microcontroller used to generate the gate signals.

This means that the second approach presented in Section III is in direct conflict with common designs for DPT circuits. It is therefore to be recommended that the simpler method reviewed in Section II should be used for a worst-case error estimation of the current sensors' impacts on a DPT setup. The extended analysis developed in Section III should only be used in those environments where L_{DPT} is similar to $(L_{par} + L_{Sensor})$.

Due to the danger of receiving implausible results, no selection aid similar to Fig. 12 and Fig. 13 is given here for this extended error analysis.

This risk of implausible results could theoretically be reduced if the averaging interval for the numerator in (32) was not selected up to τ_2, but up to the point where $\iota_{Filt,1,mod}$ reaches a certain threshold level of e.g. 99 % of the DPT current I_L. Such threshold levels are somewhat arbitrary and must be selected with great care, since a poorly selected threshold can constrain the averaging such that excessively large errors are calculated.

V. CONCLUSION

In this paper, the impact of current sensors on fast-switching WBG power semiconductor circuits in a DPT environment is investigated. Since the DPT requires a current sensor to measure the DUT's switching current, it was expected that its insertion into highly optimised circuits would influence switching loss measurements. These influences are investigated and mathematical descriptions for error estimates are derived.

In Section II, a previously published study that constructed these error estimates with worst-case approximations is translated and reviewed. Its objective was to provide a comparison of various current sensors in terms of their suitability for measuring transient DPT currents for fast-switching power semiconductors. Examples of individual current sensor error compositions are presented, along with a selection aid for available and experimental sensors.

Section III then addresses a drawback of the reviewed method, which does not consider the full switching current waveform. An extended description is developed that reduces this drawback by including the effect of the DPT storage inductance on the DUT current after this current has initially reached the desired value. This extension additionally takes measurable data into account, while the reviewed method relies on calculated circuit properties.

In Section IV, these two methods are compared. It is found that the reviewed method overestimates the actual errors, as it is based on worst-case approximations. On the other hand, the extended description may lead to implausible error estimates when the DPT storage inductance is much larger than the commutation loop inductance. Since this is the case for most DPT circuits, it is recommended to use the reviewed method of Section II as a general approach to estimate current sensor insertion errors for DPT circuits. Only in rare cases where L_{DPT} has a similar value to L_{par} and L_{Sensor} should the extended analysis of Section III be used, even though its calculation parameters are more closely related to real measurements.

Regardless of the method used, the effects described in this paper will affect any DPT measurement and should be considered when measuring switching losses in fast-switching power semiconductors. This again emphasises the need to consider the entire setup when attempting to measure ever faster transients.

Future research should explore opportunities to combine the advantages of both presented methods, by developing a compact and easy-to-use selection aid based on measureable data rather than approximations.

The methodology applied in this paper uses a general approach to signal modelling by investigating normalised mathematical functions and can therefore easily be adapted to other sensor types and measurement tasks, e.g. switching voltage measurements.

REFERENCES

[1] M. Kazanbas, A. Schittler, S. Araujo, P. Zacharias, "High-side driving under high-switching speed: Technical challenges and testing methods," in *Proc. Int. Exhib. Conf. Power Electron., Intell. Motion, Renewable Energy Energy Manage.*, 2015, pp. 1–8.
[2] S. Sprunck, M. Münch, P. Zacharias, "Transient current sensors for wide band gap semiconductor switching loss measurements," in *Proc. Int.*

Exhib. Conf. Power Electron., Intell. Motion, Renewable Energy Energy Manag., 2019, pp. 1–8.
[3] ROHM Co., Ltd, "Datasheet "SCT3060AL"," Rev. 005. [Online]. Available: https://fscdn.rohm.com/en/products/databook/datasheet/discrete/sic/mosfet/sct3060al-e.pdf
[4] GaN Systems Inc., "Datasheet "GS66516T"," Rev. 210727. [Online]. Available: https://gansystems.com/wp-content/uploads/2021/07/GS66516T-DS-Rev-210727.pdf
[5] S. Sandler, "Faster-switching GaN: Presenting a number of interesting measurement challenges," *IEEE Power Electron. Mag.*, vol. 2, no. 2, pp. 24–31, Jun. 2015, doi: 10.1109/MPEL.2015.2420232.
[6] B. Sun, Z. Zhang, M. A. E. Andersen, "Research of low inductance loop design in GaN HEMT application," in *Proc. 44th Annu. Conf. IEEE Ind. Electron. Soc.*, 2018, pp. 1466–1470, doi: 10.1109/IECON.2018.8591732.
[7] F. Yang, Z. Liang, Z. J. Wang, F. Wang, "Design of a low parasitic inductance SiC power module with double-sided cooling," in *Proc. IEEE Appl. Power Electron. Conf. Expo.*, 2017, pp. 3057–3062, doi: 10.1109/APEC.2017.7931132.
[8] E. Dechant, N. Seliger, R. Kennel, "Design of a low multi-loop inductance three level neutral point clamped inverter with GaN HEMTs," in *Proc. IEEE Energy Convers. Congr. Expo.*, 2020, pp. 3992–3997, doi: 10.1109/ECCE44975.2020.9236336.
[9] B. Sun, Z. Zhang, M. A. E. Andersen, "Research of PCB parasitic inductance in the GaN transistor power loop," in *Proc. IEEE Workshop Wide Bandgap Power Devices Appl. Asia*, 2019, pp. 1–5, doi: 10.1109/WiPDAAsia.2019.8760312.
[10] S. Hain, M.-M. Bakran, "New Rogowski coil design with a high DV/DT immunity and high bandwidth," in *Proc. 15th Eur. Conf. Power Electron. Appl.*, Lille, France, 2013, pp. 1–10, doi: 10.1109/EPE.2013.6631855.
[11] E. Hoene, A. Ostmann, B. T. Lai, C. Marczok, A. Müsing, J. W. Kolar, "Ultra-low-inductance power module for fast switching semiconductors," in *Proc. Int. Exhib. Conf. Power Electron., Intell. Motion, Renewable Energy Energy Manage.*, Nuremberg, Germany, 2013, pp. 198–205.
[12] S. Sprunck, "Charakterisierung der schaltverluste diskreter wide band gap leistungshalbleiter und entwärmung kompakter bauteile," Ph.D dissertation, Univ. Kassel, Germany, 2021, ISBN: 978-3-7376-0943-2, doi: 10.17170/kobra-202103043416.
[13] T&M Research Products, Inc., "SERIES SDN-414," Viewed on: Aug. 9, 2021. [Online]. Available: https://www.tandmresearch.com/index.php
[14] Power Electronic Measurements (PEM) Ltd., "Datasheet "CWT Mini50HF"," Feb. 2020. [Online]. Available: http://www.pemuk.com/Userfiles/cwtmini50hf/CWT_Mini50HF_DS_Feb_2020.pdf
[15] Eduard Rhein Stiftung, "For the first theoretically exact formulation of the sampling theorem," [Online]. Available: https://www.eduard-rhein-stiftung.de/en/fur-die-erstmalige-theoretisch-exakte-formulierung-des-abtasttheorems/
[16] V. A. Kotelnikov, "On conductivity of 'ether' and wire," in *Proc. Mater. Radio- Commun. 1st All-Union Conf. Problems Commun. Syst. Tech. Reconstruction*, 1933.

SEBASTIAN SPRUNCK received the B.Sc., M.Sc., and Ph.D. degrees in electrical engineering from the University of Kassel, Kassel, Germany, in 2014, 2016, and 2021, respectively.

In 2017, he started working as a Research Assistant with the Centre of Competence for Distributed Electric Power Technology, University of Kassel, where he worked on the miniaturisation of power electronic systems and on the application of wide band gap semiconductors in power electronic devices. Since 2020, he has been with Fraunhofer IEE, Kassel, Germany, with Converters and Drive Technology Department, as Group Manager Devices and Measurement Systems. He is investigating the influences of individual technological advances, such as wide band gap semiconductors, and of broader trends, such as the german Energiewende, onto power electronic components, circuits and systems. His main research interests include the characterisation and optimisation of (WBG) semiconductor switching losses and their implementation in power electronic systems.

Mr. Sprunck is a Member of the VDE Association for Electrical, Electronic and Information Technologies and of the VDI Association of German Engineers e.V.

CHRISTIAN LOTTIS received the B.Sc. and M.Sc. degrees in electrical engineering from the University of Kassel, Kassel, Germany, in 2019 and 2021, respectively.

Since August 2021, he has been a Research Assistant with the Bonn-Rhein-Sieg University of Applied Sciences, Sankt Augustin, Germany.

FABIAN SCHNABEL received the Dipl.-Ing. (FH) degree from the University of Applied Sciences Dresden (HTW Dresden), Dresden, Germany, and the M.Sc. degrees from the University of Kassel, Kassel, Germany, in 2011 and 2015, respectively, both in electrical engineering.

From 2011 to 2013, he was a Development Engineer with Technology Development Department, SMA Solar Technology AG, Niestetal. In 2013, he started working as a Research Assistant with Converters and Drive Technology Department, Fraunhofer IEE, Kassel, Germany, where he is currently Group Manager Power Electronics and Electrical Machines 2019. His current research interests include high-power grid-connected converters using new SiC and GaN semiconductors.

MARCO JUNG (Senior Member, IEEE) completed an apprenticeship for communication electronics in 2003. He received the Diploma from the TH Mittelhessen University of Applied Sciences, Giessen, Germany, the M.Sc. degrees from the University of Kassel, Kassel, Germany, in 2008 and 2010, respectively, both in electrical engineering, and the Ph.D. degree from Leibniz University Hannover, Hanover, Germany, in 2016.

Parallel to his Ph.D. studies, he started working with Fraunhofer IEE, Kassel, Germany, in 2010. Since 2017, he has been the Head of Converters and Drive Technology Department. In 2019, he additionally became a Full Professor with the Bonn-Rhein-Sieg University of Applied Sciences, Sankt Augustin, Germany. At the Institute of Technology, Resource and Energy-Efficient Engineering, he is responsible for power electronics for renewable energies and electric vehicles.

Since January 1st, 2020, he has been the Chairman of the IEEE Joint IES/IAS/PELS German Chapter. He is a Member of the International Scientific Committee (ISC) of the European Power Electronics and Drives Association (EPE) and a Member of the European Center for Power Electronics (ECPE).